Epitaxial YBa$_2$Cu$_3$O$_7$ Films on Rolled-Textured Metals for High-Temperature Superconducting Applications

Submitted to the *Journal of Materials Science and Engineering B*
4th International Workshop on Oxide Electronics

D. P. Norton, C. Park, C. Prouteau, D. K. Christen,
M. F. Chisholm, J. D. Budai
Solid State Division,
Oak Ridge National Laboratory,
P. O. Box 2008, Oak Ridge, TN 37831-6056

A. Goyal, E. Y. Sun, D. F. Lee, D. M. Kroeger, E. Specht
Metals and Ceramics Division,
Oak Ridge National Laboratory,
P. O. Box 2008, Oak Ridge, TN 37831-6033

M. Paranthaman
Chemical and Analytical Sciences Division,
Oak Ridge National Laboratory,
P. O. Box 2008, Oak Ridge, TN 37831-6100

RECEIVED
MAY 0 4 1998
OSTI

April 1998

MASTER

DTIC QUALITY INSPECTED 1

DISTRIBUTION OF THIS DOCUMENT IS UNLIMITED

19980528 033

DISCLAIMER

Epitaxial YBa$_2$Cu$_3$O$_7$ Films on Rolled-Textured Metals for High-Temperature Superconducting Applications

D. P. Norton, C. Park, C. Prouteau, D. K. Christen, M. F. Chisholm, J. D. Budai

Solid State Division, Oak Ridge National Laboratory, P. O. Box 2008, Oak

Ridge, TN 37831-6056

A. Goyal, E. Y. Sun, D. F. Lee, D. M. Kroeger, E. Specht

Metals and Ceramics Division, Oak Ridge National Laboratory, P. O. Box 2008,

Oak Ridge, TN 37831-6033

M. Paranthaman

Chemical and Analytical Sciences Division, Oak Ridge National Laboratory, P.

O. Box 2008, Oak Ridge, TN 37831-6100

Abstract

The epitaxial growth of high temperature superconducting (HTS) films on rolled-textured metal represents a viable approach for long-length superconducting tapes. Epitaxial, 0.5 μm thick $YBa_2Cu_3O_7$ (YBCO) films with critical current densities, J_c, greater than 1 MA/cm^2 have been realized on rolled-textured (001) Ni tapes with yttria-stabilized zirconia (YSZ)/CeO_2 oxide buffer layers. This paper describes the synthesis using pulsed-laser deposition (PLD) of epitaxial oxide buffer layers on biaxially-textured metal that comprise the so-called rolling-assisted biaxially-textured substrates (RABiTS^{TM}). The properties of the buffer and $YBa_2Cu_3O_7$ films on rolled-textured Ni are discussed, with emphasis given to the crystallographic and microstructural properties that determine the superconducting properties of these multilayer structures.

Introduction

Significant effort has been directed towards developing high-current superconducting wire technologies [1,2]. Much of this work has focused on achieving the crystallographic texture needed in HTS wire or tape architectures in order to realize high critical current densities at 77 K. It has been recognized for some time that randomly oriented polycrystalline HTS materials have critical current densities, J_c, < 500 A/cm^2. In contrast, oriented YBCO thin films grown epitaxially on single-crystal oxide substrates, such as (001) $SrTiO_3$, exhibit J_c values > 1 MA/cm^2 at 77 K [3]. This large difference between randomly-oriented HTS ceramics and single crystal-like epitaxial

3

films is directly related to the misorientation angles at the grain boundaries in polycrystalline materials. Values for J_c across a grain boundary decrease significantly as the misorientation angle increases, with weak-link behavior observed for grain boundary misorientation angles greater than ~10° [4]. In order to achieve high critical current densities (~10^6 A/cm^2, 77 K), the HTS superconducting wire or tape must possess a high degree of both in-plane and out-of-plane grain alignment over the conductor's entire length. Preferably, this would be achieved with YBCO, because the limits for dissipation-free current at 77 K in an applied magnetic field are most favorable for this material [5,6].

Two deposited HTS conductor approaches have recently received significant attention as a means of producing long-length HTS tapes possessing the in-plane and out-of-plane crystallographic texture necessary for high values of J_c. One technique, known as ion beam-assisted deposition (IBAD), utilizes an ion beam to induce in-plane alignment of a depositing film as is schematically illustrated in Fig. 1 [7,8]. Related techniques that also utilize energetic ions to induce crystallographic orientation in polycrystalline films include PLD with inclined substrates [9] and bias sputter deposition [10]. With these energetic ion-assisted approaches, only the film possesses significant crystallographic texture, with the crystallinity of the supporting substrate material assumed to be irrelevant. This technique offers significant flexibility in substrate choice, and has been shown effective for a variety of thin film and substrate materials. However, the necessity of an ion beam in

4

processing long length conductors is generally viewed as a disadvantage. An alternative approach also shown in Fig. 1 involves the formation of crystallographic texture through mechanical deformation and subsequent recrystallization of a metal substrate (11). The deposition of appropriate epitaxial buffer layers on the biaxially-textured metal results in an oriented architecture known as a rolling-assisted biaxially-textured substrate (RABiTS™) [12,13]. The RABiTS™ approach is obviously restricted to metals for which advantageous crystallographic texture can be achieved through thermo-mechanical deformation. A key advantage of this approach is in the simplicity of producing the initial in-plane alignment required for high J_c by a cold-rolling and annealing process that can be easily scaled to produce arbitrary substrate lengths. In this paper, we review the synthesis and properties of superconducting RABiTS™ using pulsed-laser deposition, and discuss recent microstructural characterization of these structures

RABiTS™ Process for HTS Conductors

The specific implementation of the RABiTS™ approach that has produced HTS films with high values of J_c utilizes a biaxially textured (001) Ni tape, formed by recrystallization of cold-rolled pure Ni [11], as the initial, in-plane aligned substrate. Smooth Ni tapes that are 25–125 μm thick have been produced possessing a relatively sharp cube orientation with a FWHM out-of-plane texture $\Delta\theta$ ~6°–10° and an in-plane texture $\Delta\phi$ ~6°–15°, depending on the specific rolling and annealing conditions, as well as material purity, with

5

a grain size ranging from ~30–100 μm in diameter. A (001)-oriented oxide buffer layer architecture is then epitaxially grown that maintains the sharp crystallographic cube texture of the metal substrate while providing a barrier to chemical interaction with the Ni. Typically, the epitaxial growth of any (001)-oriented cubic oxide on a (001) Ni surface is inhibited by the formation of (111) NiO at the oxide/metal interface [14]. In order to suppress the formation of NiO and achieve (001)-oriented epitaxy directly on the (001) Ni surface, H_2 gas is introduced into the PLD chamber during the initial stages of CeO_2 growth. Hydrogen is effective in reducing NiO, while having little effect on the CeO_2 film. The nucleation of the CeO_2 layer in the presence of H_2 results in the formation of (001) CeO_2, with subsequent growth in either vacuum or a background of oxygen maintaining this orientation. Similar results for CeO_2 on (100) Ni have been achieved using both sputtering [15] and e-beam evaporation [16]. This (001)-oriented CeO_2 layer provides an oxide template directly on the metal surface for the subsequent epitaxial growth of additional oxide buffer and HTS layers.

Crystallographic Properties

The local crystallographic texture for a $YSZ/CeO_2/Ni$ tape as determined by electron back-scattered patterns (EBSP) is shown in Fig. 2. A YSZ layer has proven useful in alleviating cracking of the oxide layers that often occurs due to the thermal expansion mismatch between the Ni substrate and the oxides. Figure 2(a) shows an image of a typical film grown by PLD. The location of the grain boundaries from the Ni grains are clearly evident in the

6

morphology due to thermal grooving of the Ni during annealing. The horizontal and vertical lines are residual cracks that appear along the (110) planes in the CeO_2 layer. Figure 2(b) is a shaded map of the local texture determined with EBSP in which a change in crystal orientation greater that 1° is indicated by a change in shading. Within each Ni grain, the orientation of the CeO_2 and YSZ grains is uniform to within 1°, which is consistent with epitaxy of the oxides on the (001) Ni surface. Figure 2(c) is a similar plot in which the point-to-point orientation criterion for shade change is 5°. For the region shown, the Ni grains are textured to within 5°, with this texture reproduced in the oxide buffer layers. This figure clearly illustrates that the orientation in the Ni substrate can be reproduced in the subsequent buffer layers.

The θ–2θ x-ray diffraction (XRD) scan of a YBCO/YSZ/CeO2/Ni composite structure in Fig. 3 shows that the CeO2 and YSZ buffer layers, as well as the YBCO layer, are (001)-oriented relative to the surface normal. The XRD rocking curve through the Ni (002) peak shown in Fig. 4 reveals a significant amount of structure, due to the coarse-grained nature of the rolled-textured substrate, yielding an out-of-plane FWHM of ~6° for the sample considered. Subsequent rocking curves through the (002) peaks for the CeO2 and YSZ layers indicate an out-of-plane FWHM of 5.5° and 5°, respectively. Some structure is also observed in these rocking curves, reflecting the good epitaxial relationship between the oxides and the underlying Ni grains. A significant narrowing in the out-of-plane texture is observed for the YBCO when

7

deposited directly on the YSZ layer, with the rocking curve through the (005) YBCO peak yielding an out-of-plane FWHM of only 1°. This improvement in the out-of-plane alignment relative to the underlying Ni results from the low (001) surface energy and the anisotropic film growth nature commonly observed for YBCO. Also shown is the in-plane crystallographic alignment of the epitaxial YBCO/YSZ/CeO$_2$/Ni structure as determined by XRD ϕ-scans through the YBCO (226), YSZ (202), CeO$_2$ (202), and Ni (222) peaks. The in-plane FWHM for all of the layers is ~6.8°, indicating excellent epitaxy of the oxide layers with the biaxially textured metal. If the grain-to-grain misorientation angles are uncorrelated with a normal distribution, ~90% of the Ni grains have in-plane misorientation angles of 7° or less for this sample [17]. Note that the in-plane (100) CeO$_2$ and YSZ principal crystallographic axes are rotated 45° relative to the in-plane (100) Ni axis, whereas the a- and b- axes of the YBCO are rotated 45° with respect to the YSZ axes, all of which are in agreement with near-coincidence site lattice models [18].

One important factor to consider for the YBCO/YSZ/CeO$_2$/Ni architecture involves the in-plane orientation of the YBCO films on the YSZ layers. Due to a large lattice mismatch, two distinct in-plane orientations of YBCO on (100) YSZ are often observed. The presence of two in-plane orientations leads to 45° grain boundaries and a subsequent reduction in J_c. Previous work has shown that various oxide buffer layers, including CeO$_2$, can significantly suppress one of these orientations [19]. By growing YBCO/CeO$_2$/YSZ/CeO$_2$/Ni structures with a thin (~200Å) CeO$_2$ cap layer on

8

the YSZ, improvement in the reproducibility of J_c has been observed, with YBCO films routinely obtained on RABiTS™ substrates with only one in-plane orientation.

Superconducting Transport Properties

Using pulsed-laser deposition, c-axis oriented, in-plane aligned YBCO has been obtained on RABiTS™ substrates with T_c ~87–90 K and J_c(77 K) as high as 1.4 MA/cm² for 0.5 μm thick films. Figure 5 shows J_c(77 K) as a function of magnetic field applied parallel to the YBCO c-axis for a film deposited on a RABiTS™ substrate. For this film, J_c(77 K, H = 0) ~1.2 MA/cm². The J_c behavior for the YBCO films on the rolled-textured Ni tapes is comparable with that observed for epitaxial films on oxide single crystals, which is consistent with the absence of high angle grain boundaries in the YBCO film. In addition, YBCO films on RABiTS™ substrates typically exhibit very strong flux pinning as indicated by the field dependence of J_c. At high fields, these films can be superior to epitaxial films on single crystal (001) SrTiO₃ as observed in Fig. 5 for H > 3 Tesla. For comparison, we also indicate the J_c(77 K, H) behavior for epitaxial Bi-2212 and TlBi-1223 [20] films on single crystal substrates to illustrate the performance advantage of YBCO on RABiTS™ relative to other HTS systems.

Engineering Issues for RABiTS-Based HTS Conductors

The use of thinner (001) Ni tapes holds the promise of achieving high engineering critical current densities (J_e) with 1–2 μm thick YBCO films.

9

Previous results have shown that Ni could be rolled-textured to a thickness of ~25 μm with in-plane and out-of-plane texture similar to that obtained for 125 μm thick Ni tapes. Initial efforts have focused on the epitaxial growth of the YBCO/YSZ/CeO$_2$ oxide architecture on 25 μm-thick Ni tapes using pulsed-laser deposition. Four-circle x-ray diffraction for the YBCO/YSZ/CeO$_2$ oxide architecture on 25 μm Ni shows that the oxide layers are epitaxial and in-plane aligned with respect to the Ni substrate. The best result achieved to date with 25 μm thick Ni substrates is J_c(77 K) ~200 kA/cm^2, yielding an engineering J_c of 11.5 KA/cm^2. Significantly higher values for J_c are anticipated as superior procedures for handling these relatively thin metal tapes are developed. Future efforts will also focus on understanding the effect of substrate thickness on the conductor properties, particularly when considering the difference in thermal expansion for the oxides layers and the thin Ni tape.

Another important aspect for any HTS wire technology involves the degree to which the conductor can be bent without damaging the conductor. To address this issue, bend strain tolerance measurements of J_c have been performed on RABiTS™ structures. The bend strain tolerance for two YBCO/buffer layers/Ni tapes measuring tensile and compressive strain tolerance is shown in Fig. 6. For both of these samples, the buffer layers and YBCO were deposited using PLD. The samples were placed in strain by deforming the tapes over a selected radius of curvature at room temperature. The strain is then removed (sample curvature is removed) for J_c

measurement in liquid nitrogen. Each data point in the plot represents bending, straightening and thermal cycling. The initial J_c(77 K) for each sample was greater than 0.5 MA/cm^2. For compressive strain, significant degradation of J_c was not observed until the bend strain exceeded 0.7%, at which point failure was catastrophic. Scanning electron microscopy images of this sample after strain tolerance measurements indicate the presence of long cracks that extend a significant fraction of the sample width. The observation of long cracks in the YBCO film is consistent with the catastrophic failure that was observed in the behavior of J_c. For the case of tensile strain, a significant decrease in J_c with applied strain began at ~ 0.3 %. In contrast to the behavior observed for compressive strain, failure of the sample with tensile strain was more gradual, with complete failure ($J_c = 0$) observed for a strain of ~0.5%. The SEM micrograph for this sample shows an array of short fracture lines with the density of cracks higher for the tensile strain than for the sample placed in compression. The appearance of short cracks is consistent with a gradual failure of the film for tensile strain. Future efforts will continue to focus on the effects of specific multilayer oxide architectures on the strain tolerance.

Microstructure of Epitaxial YBCO / Buffer Layers / Ni

A fundamental understanding of the epitaxial oxide / metal micro-structure is crucial in efforts to effectively characterize and further improve the performance of RABiTS™-based HTS conductors. Microstructural issues that need to be addressed include microcracking, secondary phase nucleation,

11

film growth over Ni grain boundary grooves, and substrate oxidation. The scanning electron microscopy image of a YSZ/CeO$_2$/Ni sample shown in Fig. 7 illustrates some of these features. The grooves at the Ni grain boundaries may impact the nucleation of the CeO$_2$ on the Ni surface. One must also consider the YBCO growth across this macroscopic surface feature. In addition, the microcracks that often appear in the CeO$_2$ layer must be reduced or eliminated in order to maximize the ability of the HTS film to carry currents. Note also the appearance of NiO rods that grow through pinholes in the buffer layers. The presence of these outgrowths provide a source for local nickel contamination of the YBCO film as well as strain in the buffer layer that could lead to additional cracking and perhaps delamination.

Microstructural characterization using cross-section transmission electron microscopy (TEM) has been performed on several YBCO/buffer layer/Ni structures. Figure 8 shows results from a cross-section TEM image of a YBCO/YSZ/CeO$_2$/Ni sample. This cross-section reveals each of the oxide layers and includes a grain boundary that originates from the Ni substrate. There are several features of interest in this micrograph. First, significant oxidation of the nickel substrate is evident at the Ni/CeO$_2$ interface with a NiO layer thickness of 100–400 Å. It is assumed that this NiO layer forms after the nucleation of (100) CeO$_2$ on the (100) Ni surface. The formation of a NiO layer at the metal/oxide layer interface should have significant influence on the mechanical and adhesive properties of the film due to stresses related to the volume change with the oxidation of Ni at the buried interface. High

resolution TEM of the NiO/Ni and NiO/CeO$_2$ interfaces shown in Fig. 9 shows that the NiO is epitaxial with a 45° rotation of the CeO$_2$ principle axes with respect to the NiO.

The cross-section of the CeO$_2$ layer shown in Fig. 10 reveals three distinct microstructures that correspond to changes in the film growth conditions during the initial nucleation and subsequent growth of the CeO$_2$ layer. The initial CeO$_2$ is deposited in the presence of Ar/H$_2$ as pointed out earlier. This results in a somewhat uniaxial microstructure. After the nucleation of ~300 Å, the Ar/H$_2$ background gas is evacuated while continuing to deposit an additional 500 Å of CeO$_2$. This growth in a background pressure of ~10^{-5} Torr results in a more columnar microstructure. This is then followed by growth in an oxygen pressure of 4×10^{-4} Torr which again results in a more uniaxial microstructure.

The microstructure of the YSZ layer is distinctly columnar as indicated in Fig. 11. Some evidence for a BaZrO$_3$ layer at the YBCO/YSZ interface is observed, although the thickness of this interaction layer is minimal. One interesting issue regards how the groove at the Ni grain boundary is accommodated in the various layers. From Fig. 8, we observed that the morphology of the groove is reproduced in each of the oxide layers. Figure 11 shows that the orientation of the columnar microstructure within the YSZ layer follows the morphology of the groove. With this macroscopic change in local microstructure, one might anticipate significant disruption of the YBCO epitaxy across this feature based on the tendency of YBCO to align the c-axis

perpendicular to the growing surface, as well as the behavior of YBCO epitaxy across etched steps on single crystal surfaces. This could prove detrimental to transport with the local formation of large angle grain boundaries across the groove. Fortunately, this does not appear to be the case. Deep within the groove, the epitaxy of YBCO appears to be disrupted. However, the YBCO grains adjacent to the groove apparently grow over the grooved region. Note that the grain boundary location, while effectively translated vertically within the buffer layer architecture, has shifted laterally to the edge of the groove. An explanation for this observation is that the YBCO grains that nucleate on flat regions of the substrate dominate film growth leading to overgrowth over the grooved region. This is consistent with previous bicrystal experiments in which significant meandering of the YBCO grain boundary is observed with respect to the location of the grain boundary in the underlying bicrystal substrate.

Plan-view Z-contrast scanning transmission electron microscopy (Z-STEM) provides additional insight regarding the atomic structure of the YBCO grain boundaries for films deposited on these substrates. Figure 12 shows an atomic resolution Z-STEM image of a typical YBCO low-angle grain boundary that is commonly observed in c-axis oriented YBCO films deposited on rolled-textured (001) Ni tape. These low-angle grain boundaries in epitaxial YBCO film on RABiTS™ originate from the grain structure in the biaxially-textured (001) Ni tape. As seen in the figure, the atomic structure of the grain boundary closely resembles that observed for YBCO films on $SrTiO_3$

bicrystals, consisting of a "clean" boundary with a regular array of dislocation cores. From the micrograph, there is no evidence for impurity phases, NiO, or misoriented YBCO grains at the boundary. This is consistent with the relatively high critical currents that are observed for YBCO/buffer layers/(001) biaxially textured Ni structures.

Conclusion

The use of biaxially-textured substrates for HTS film growth opens up an array of large-area HTS film applications, including the synthesis of superconducting YBCO tapes for high-field applications at 77 K. Epitaxial YBCO films with $J_c > 1MA/cm^2$ at 77 K have been realized on rolled-textured Ni tapes. A better understanding of metal oxide/metal epitaxial systems is needed in order to fully characterize and further improve the performance of this coated-conductor architecture in progressing from laboratory-scale samples to useful conductor lengths.

ACKNOWLEDGEMENTS

REFERENCES

1. J. W. Ekin, K. Salama, V. Selvamanickam, *Nature* 350, 26 (1991).

2. D. T. Shaw, *MRS Bull.* 17, 39 (1992); E. E. Hellstrom, *ibid.* 17, 45 (1992).

3. J. M. Phillips, *J. Appl. Phys.* **79**,1829 (1996).

4. D. Dimos et al., *Phys. Rev. Lett.* **61**, 1653 (1988).

5. D. K. Christen et al., in AIP Conf. Proc., Superconductivity and its Applications **273**, 24 (1993).

6. M. Rupp, A. Gupta, C. C. Tsuei, *Appl. Phys. Lett.* **67**, 291 (1995).

7. Y. Iijima, N. Tanabe, O. Kohno, and Y. Ikeno, *Appl. Phys. Lett.* **60**, 769 (1992).

8. X. D. Wu et al., *Appl. Phys. Lett.* **67**, 2397 (1995).

9. K. Hasegawa et al., *Proc. of the 9th Intl. Symp on Superconductivity (ISS"96)*, Oct. 1996, Sapporo, Japan.

10. M. Fukutomi et al., *Physica C* **231**, 113 (1994).

11. H. Makita, S. Hanada, O. Izumi, *Acta Metall.* **36**, 403 (1988).

12. D. P. Norton et al., *Science* **274**, 755 (1996)

13. A. Goyal, et al., *Appl. Phys. Lett.* **69**, 1795 (1996).

14. N. N. Khoi, W. W. Smeltzer, J. D. Embury, *J. Electrochem. Soc.* **122**, 1495 (1975).

15. Q. He et al., *Physica C* **275**, 155 (1997).

16. M. Paranthaman et al., *Physica C* **275**, 266 (1997).

17. E. D. Specht et al., *Physica C* **226**, 76 (1994).

18.   J. D. Budai, R. T. Young, B. S. Chao, *Appl. Phys. Lett.* **62**, 1836 (1993).

19.   D. K. Fork, S. M. Garrison, M. Hawley, and T. H. Geballe, *J. Mater. Res.* **7**, 1641 (1992).

20.   L.P. Guo, Z. F. Ren, J.Y. Lao, J. H. Wang, D. K. Christen, C.E. Klabunde, J.D. Budai, *Physica C* **277**, 13 (1997).

Figure Captions

Figure 1.   Schematic of the IBAD and RABiTS™ processes for fabricating biaxially-textured coated HTS conductors.

Figure 2.   Electron baskscattered images of epitaxial YSZ/CeO$_2$ epitaxial layers on rolled-textured Ni showing the morphology (a) as well as the crystallographic texture of a typical RABiTS™ sample. The point-to-point shading criteria for a change in grey-scale shading is (b) 1° and (c) 5°.

Figure 3.   X-ray diffraction θ-2θ scan of a YBCO/YSZ/CeO$_2$/Ni structure showing the c-axis orientation of the buffer and YBCO layers.

Figure 4.   X-ray diffraction scans showing the in-plane and out-of-plane texture for a typical YBCO/YSZ/CeO$_2$/Ni sample.

Figure 5.   The magnetic field dependence of J_c(77 K) for a 0.6 μm thick YBCO film on a YSZ/CeO$_2$/ rolled Ni substrate. The J_c(77 K, H) behavior for YBCO on (001) SrTiO$_3$ as well as for epitaxial Bi-2212 and TlBi-1223 films is also shown for comparison.

Figure 6.   Strain tolerance data for YBCO on RABiTS™ samples measured at 77 K.

Figure 7.   A scanning electron microscopy image of a YSZ/CeO$_2$/rolled Ni sample indicating the location of Ni grain boundaries, micorcracks due to thermal expansion mismatch, and NiO protrusions.

Figure 8.   A cross-section transmission electron microscopy image of a YBCO/YSZ/CeO$_2$/rolled Ni sample. The total CeO$_2$ layer thickness is approximately 900 nm.

Figure 9.   A high-resolution transmission electron microscopy image of the Ni/NiO and NiO/CeO$_2$ epitaxial interfaces.

Figure 10.   A cross section transmission electron microscopy image of the CeO$_2$ layer, with the varying microstructure corrsponding to background ambients of (a) 200 mTorr Ar/H$_2$, (b) vacuum, or (c) 4x10^{-4} Torr O$_2$.

Figure 11.   Cross-section transmission electron microscopy image of the YSZ layer showing a columnar microstructure and location of the grain boundary.

Figure 12.   A plan-view Z-contrast scanning transmission electron microscopy image of a YBCO film on a RABiTS™ substrate showing the grain boundary.

Figure 1

(a)
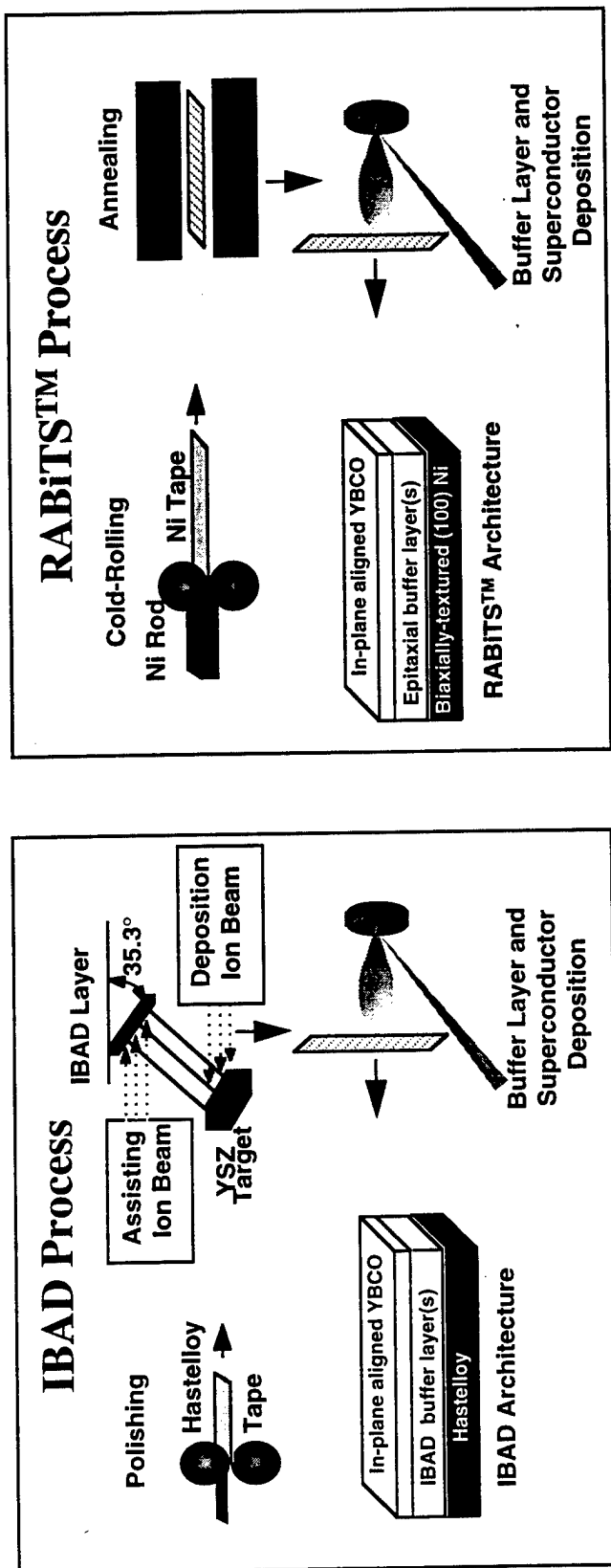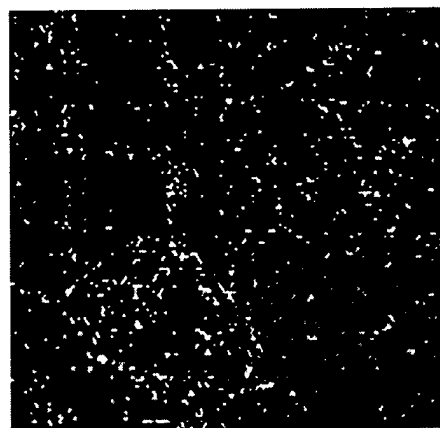
18 μm
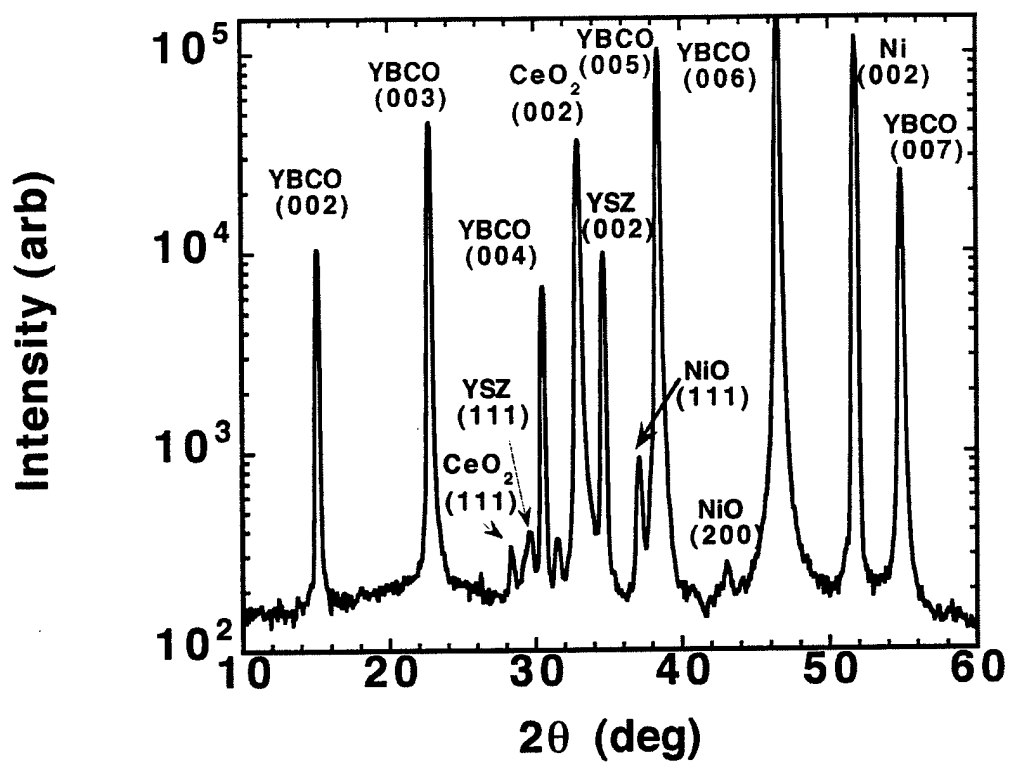
Figure 2
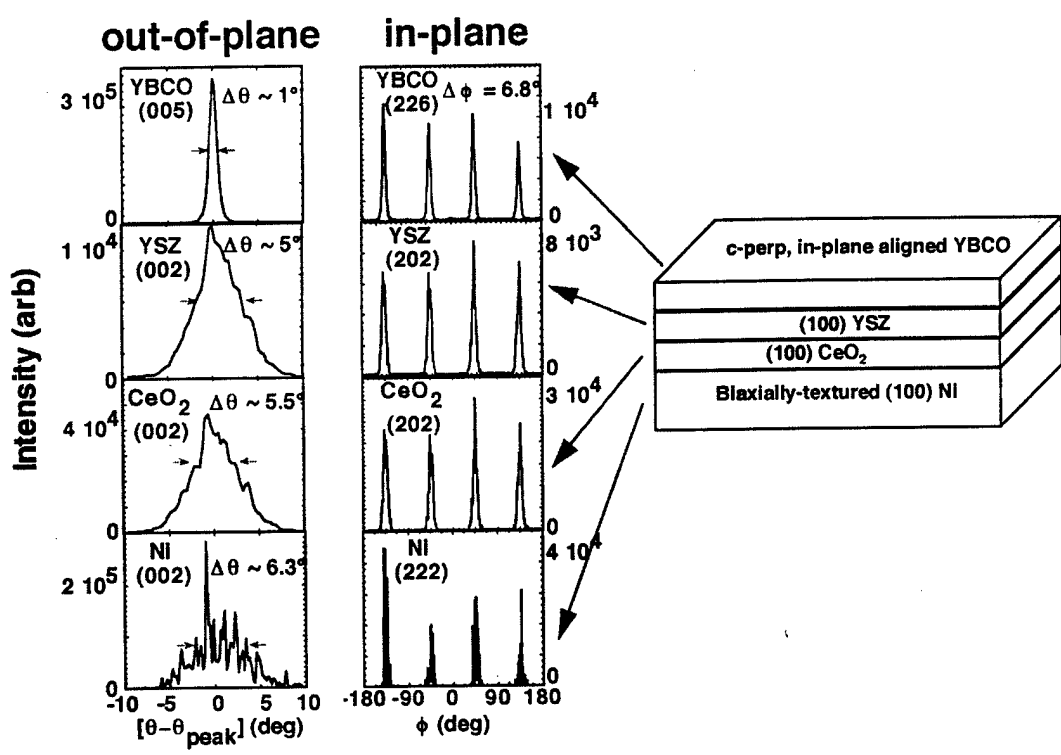
Figure 3

Figure 4
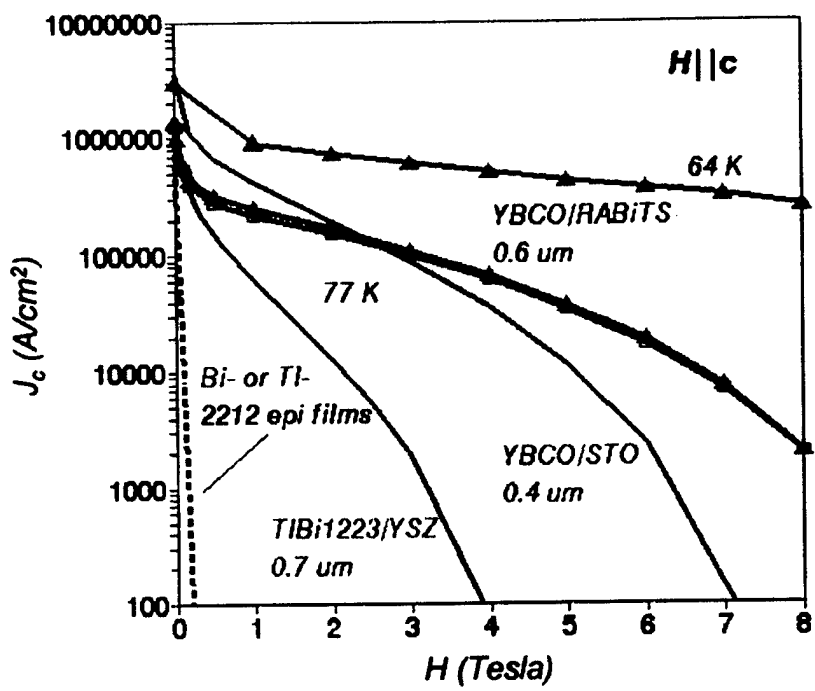
Figure 5

Fig 5

crack due to
compressive
stress
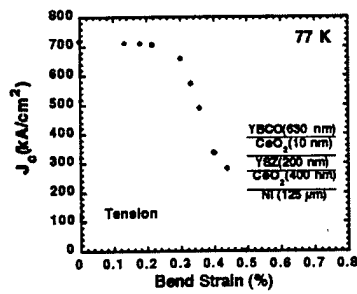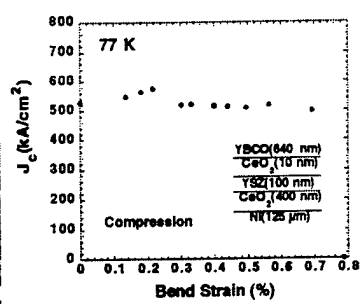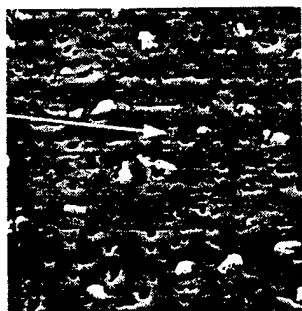
crack due to
tensile stress

Figure 6

Ni grain boundary

NiO

microcracks

18 μm

Figure 7

YBCO

YSZ

CeO_2

Ni

grain boundary

Figure 8

Figure 9

CeO$_2$ (c)

CeO$_2$ (b)

CeO$_2$ (a)

NiO

Ni
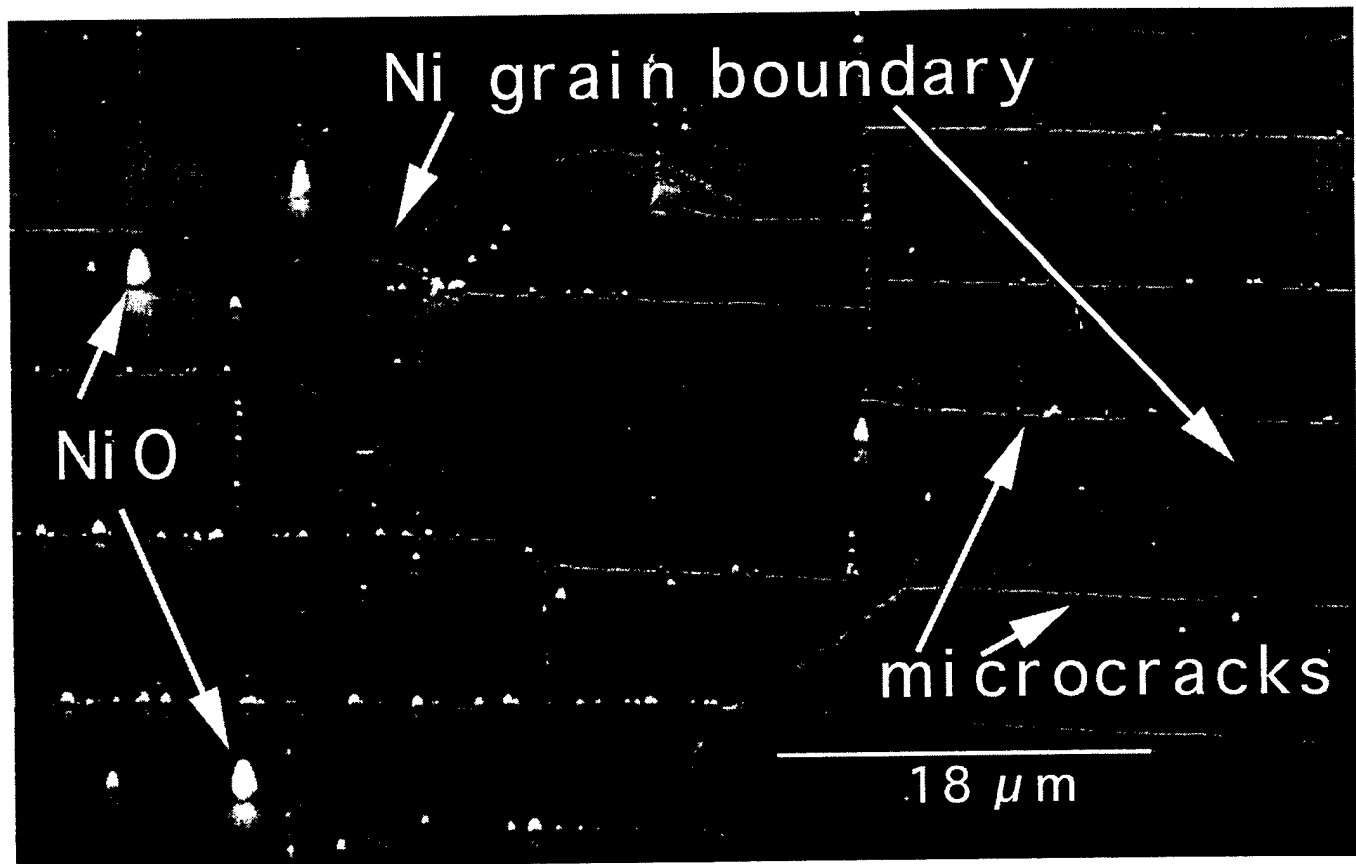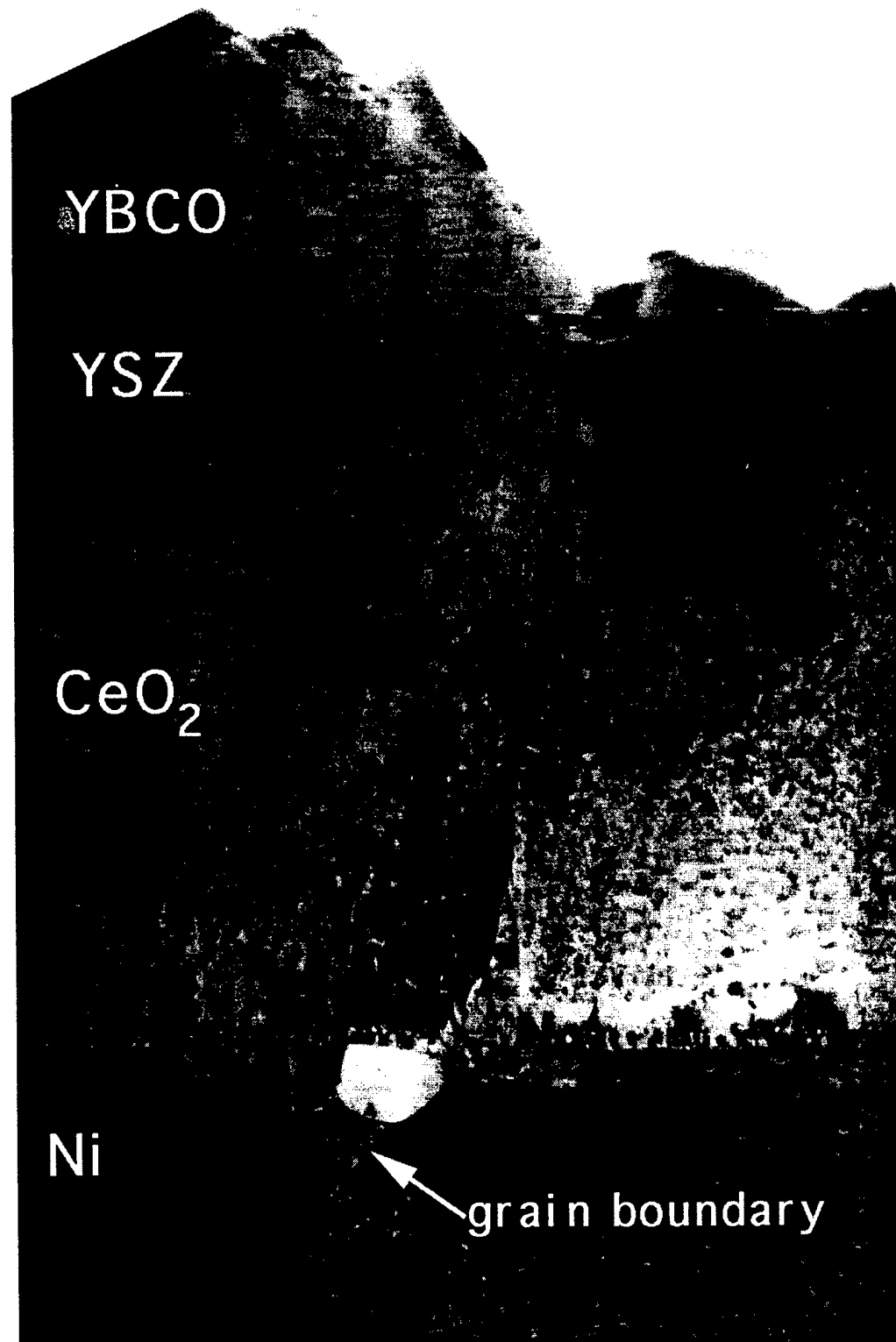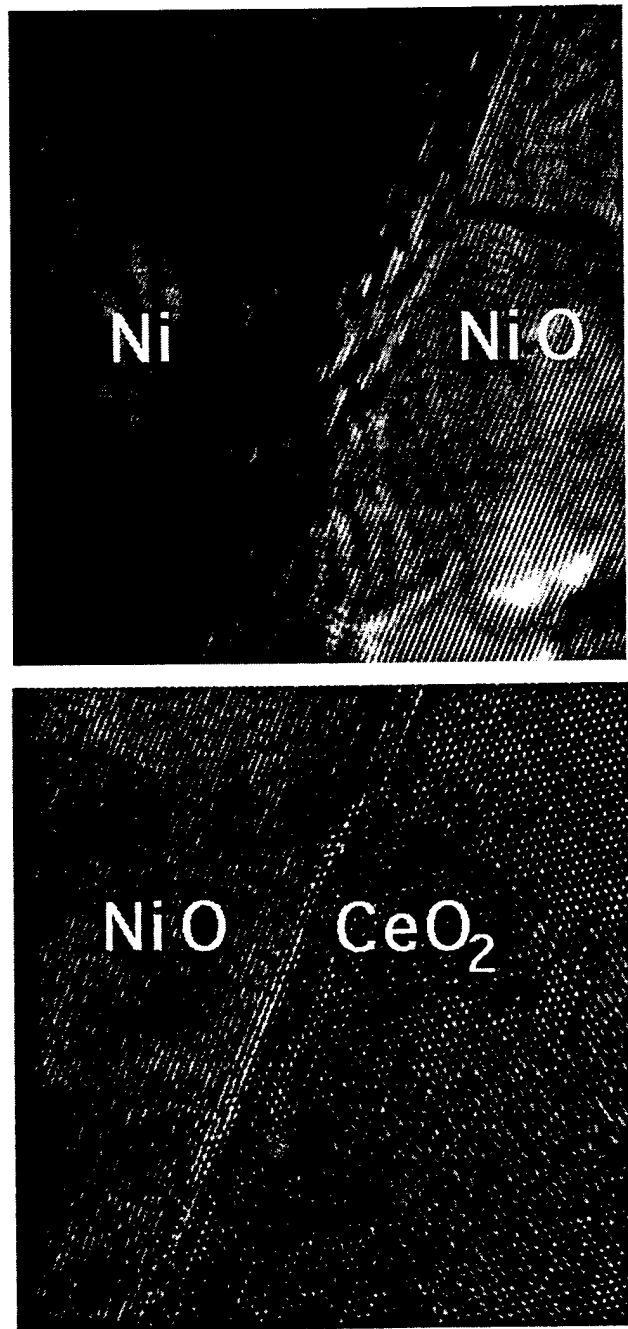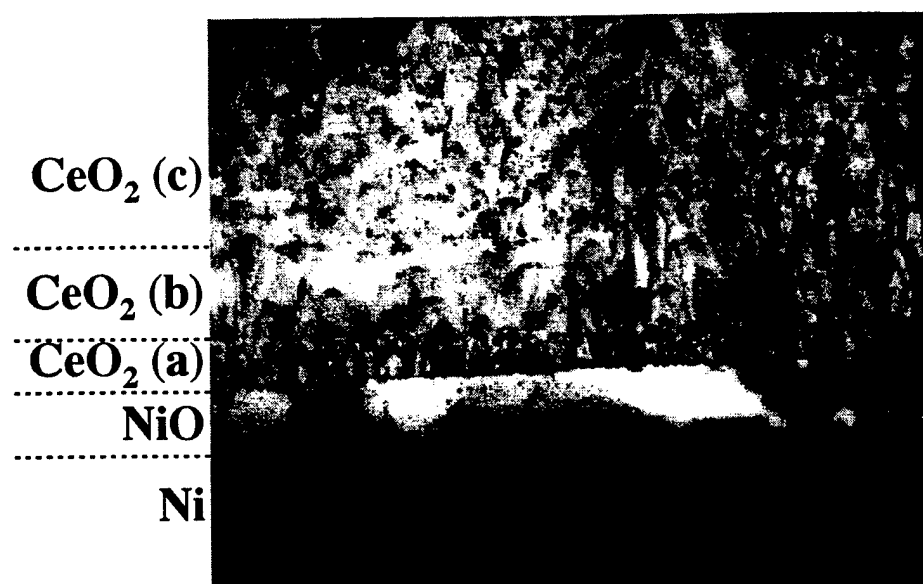
Figure 10

Figure 11

grain
boundary
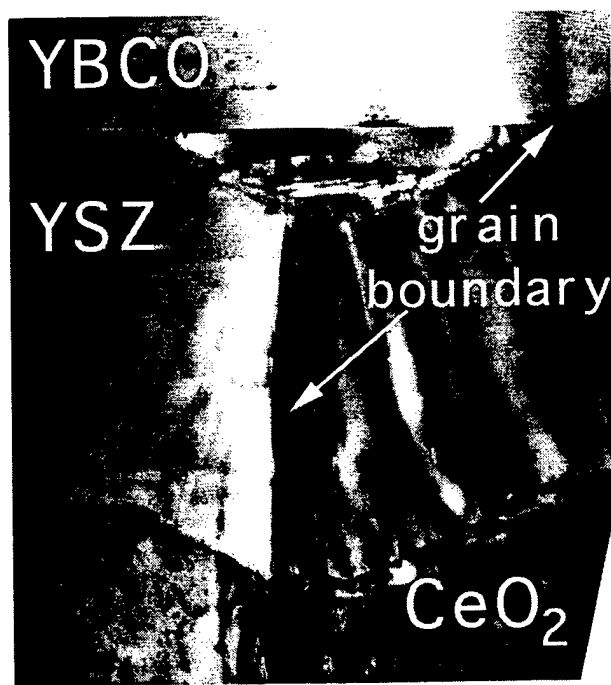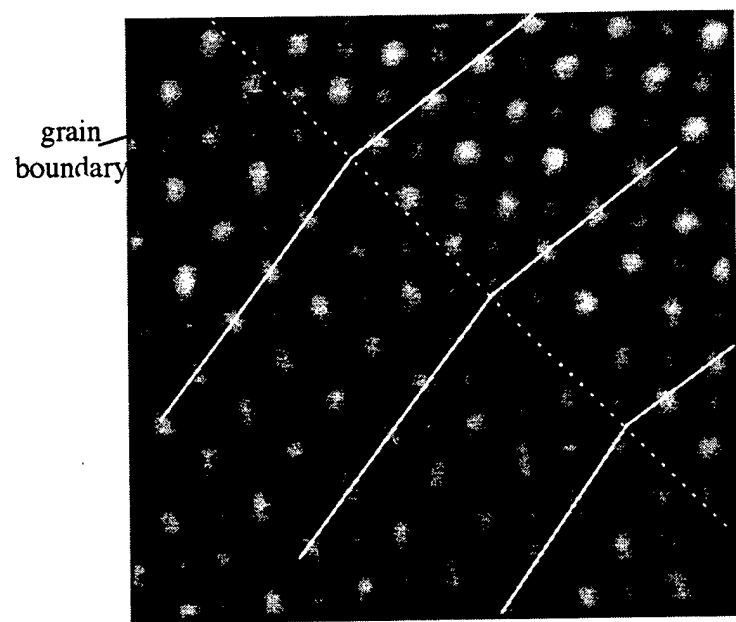
Figure 12

Report Number (14) *ORNL/CP--97526*
CONF-971236--

Publ. Date (11) *199804*
Sponsor Code (18) *DOE/ER , XF*
UC Category (19) *UC-404 , DOE/ER*

DOE